Published in final edited form as:
*Conf Comput Vis Pattern Recognit Workshops*. 2008 July 15; 2008: 1–7. doi:10.1109/CVPRW.2008.4563013.

# A Multiple Geometric Deformable Model Framework for Homeomorphic 3D Medical Image Segmentation

**Xian Fan**, **Pierre-Louis Bazin**, **John Bogovic**, **Ying Bai**, and **Jerry L. Prince**
Johns Hopkins University, Baltimore MD 21218

## Abstract

This paper presents a 3D segmentation framework for multiple objects or compartments embedded as level sets. Thanks to a compact representation of the level set functions of multiple objects, the framework guarantees no overlap and vacuum, and leads to a computationally efficient evolution scheme largely independent of the number of objects. Appropriate topology constraints ensure not only that the topology of each object remains the same, but that the relationship between objects is also maintained. The decomposition of objects makes the framework specifically attractive to the segmentation of related anatomical regions or the parcellation of an organ, where relationships must be maintained and different evolution forces are needed on different parts of the objects interface. Examples of 3D whole brain segmentation and thalamic parcellation demonstrate the potential of our method for such segmentation tasks.

## 1. Introduction

Image segmentation of anatomical structures is a fundamental and challenging problem in medical image analysis. The segmentation result often directly affects subsequent tasks such as quantification, registration and visualization. In many cases, the simultaneous segmentation of multiple objects is required—e.g., in whole brain segmentation [16]—while at the same time due to the anatomy of human organs, the topology of each object and the topological relationship between all the objects should be the same for different subjects. As well, overlap of and vacuum between the objects should be avoided, so that each voxel is assigned to one and only one object. Some tasks in medical imaging also require the segmentation of images with little or no visible boundary between different parts, requiring the inference of likely boundaries from the group structure of the objects [18, 27].

Active contours methods [23] have been exploited in image segmentation for many years, both in parametric and geometric deformable models (cf. [30, 9]). Geometric deformable models, made possible by the level set theory [31], are more flexible in topology and avoid self-intersection by embedding the evolving curve/surface in a higher dimension. However, as the topology is prescribed by anatomical knowledge in medical images, it is often desirable to regain control of the topology. Han et al. [40] introduced a digital simple point criterion to ensure that no topological changes occur during the evolution of a levelset. Several recent works have enhanced this framework through improved resolution [5], selective topology control [14], topology correction [39, 15], and through a more global topology perspective [33]. However, none of these can simultaneously maintain the topology of a group of objects, thus guaranteeing a strict homeomorphism, as illustrated in Fig. 1.

---

There are a number of multiple region segmentation methods [22, 13, 2, 26, 6, 8, 20, 3, 17, 34], most of which use $N$ level set functions to segment $N$ objects, relying on coupling forces to avoid overlaps and vacuums [6, 26, 17, 8, 4]. These energy-based methods discourage but do not guarantee the absence of overlaps and vacuums, and their performance depends on the relative weights between other terms in the formulation. The multiphase method [22] was proposed to segment $N$ regions with $\log(N)$ level set functions based on the Mumford-Shah model [11], guaranteeing no overlaps or vacuums between objects. However, since it is derived from the region-based Chan-Vese model [35], no boundary information can be explicitly incorporated other than the overall length of the zero level sets, which may actually lead to a false segmentation since it does not minimize the length of the object boundary [38]. A probabilistic embedding was proposed to avoid overlap and vacuum by replacing the level set isocontours with a labeling of regions according to their maximum probability [20]. Both methods remove overlaps and vacuums, but restrict the type of boundary information that can be exploited in the segmentation algorithm. None of the multiple level set segmentation methods maintain the topology of either a single object or a group of objects.

In this paper, we introduce a multiple object segmentation framework, which 1) guarantees no overlaps or vacuums, 2) can preserve the topology of all objects and groups of objects, 3) can apply any existing type of force in the level set literature with different weights of forces on different parts of one object, and 4) evolves only two level set functions and two label functions in two dimensions or three level set functions and three label functions in three dimensions—independently of how many objects are to be segmented. This framework extends the theory from 2D [38] to 3D. Here, we also demonstrate the theoretical and practical advantages of this framework for the simultaneous segmentation of the whole brain into ten structures and for the parcellation of the thalamic nuclei.

## 2. Theory

### 2.1. Level Set Decomposition

Let $\varphi_i$, $i = 1, 2, \ldots, N$ be the level set functions of $N$ objects that parcellate an image $I$, where the background (if it exists) is also treated as an object. By convention, these functions are signed distance functions that are positive inside their respective objects (cf. [32, 19]) and negative outside. We seek an evolution of the level set functions to minimize an energy function

$$\mathbf{E}(\varphi, I)=\sum_i \mathbf{E}_{\text{int}}(\varphi_i)+\mathbf{E}_{\text{ext}}(\varphi_i, I)+\mathbf{E}_{\text{prior}}(\varphi_i, \mathcal{P}). \tag{1}$$

where $E_{\text{int}}$, $E_{\text{ext}}$ and $E_{\text{prior}}$ are internal, external and prior shape energies, respectively. Solution by gradient descent permits us to think of the energy derivatives—e.g., $\frac{\partial E_{\text{int}}}{\partial t}$ — as forces that “push” the objects around in space. Internal energy forces encourage smoothness of the zero level set based on its curvature or length [31, 36]. External energy forces—e.g., region forces, balloon forces, gradient forces, etc. [7, 35]—encourage the level set to conform to the underlying image. Prior shape forces guide the objects toward specific shapes or classes of shapes that are expected [10, 37, 25, 24].

In the context of multiple level sets, if we want to segment the image into $N$ compartments with no overlaps or vacuums, we must preserve the mutual boundary between objects. In 3D, neighboring objects can be connected by a surface, a curve, or a point. We will consider the simplifying condition that there can be only three objects connected by a line and four objects connected by a point, a condition that is usually satisfactory in the segmentation of anatomy.

Let us consider the most general case of four objects $O_i$, $O_j$, $O_k$, and $O_l$. Suppose the distance from a region $O_j$ to a point $x$ where $L(x) \neq j$ is the smallest distance of all the points in $O_j$ to $x$. At every point $x$, we define the label functions $L$, $F$, $S$ and $T$ as

$$\begin{array}{lll} L: & L(x)=i & \text{if } x \in O_i; \\ F: & F(x)=j & \text{if } O_j \text{ first closest neighbor to } x; \\ S: & S(x)=k & \text{if } O_k \text{ scond closest neighbor to } x; \\ T: & T(x)=l & \text{if } O_l \text{ third closest neighbor to } x; \end{array} \tag{2}$$

where $O_j$ being the first closest neighbor to $x$ means that of all the regions except $O_{L(x)}$, the distance from $O_j$ to $x$ is smaller than any other regions. Similarly, the second/third closest neighbor means this distance is the second/third smallest. Using these labels, we introduce three distance-derived functions $\phi_L$, $\phi_F$, and $\phi_S$ as

$$\begin{gathered} \phi_L = \textstyle\sum_{i=1}^{N} \max\{\varphi_i, 0\}, \\ \phi_F = \textstyle\sum_{i,j=1,i\neq j}^{N} \max\{\varphi_{ij}, 0\} - \max\{\varphi_i, \varphi_j, 0\}, \\ \phi_S = \textstyle\sum_{i,j,k=1,i\neq j\neq k}^{N} \max\{\varphi_{ijk}, 0\} - \max\{\varphi_{ij}, \varphi_{jk}, \varphi_{ki}, 0\} + \max\{\varphi_i, \varphi_j, \varphi_k, 0\}, \end{gathered} \tag{3}$$

where $\varphi_{ij}$ and $\varphi_{ijk}$ are the signed distance functions for $O_i \cup O_j$ and $O_i \cup O_j \cup O_k$, respectively. These functions have a geometric meaning, corresponding to a decomposition of the distance functions inside the objects ($\phi_L$) and at the boundary between two ($\phi_F$ ) and three ($\phi_S$) objects. The decomposition into $L$, $F$, $S$ and $T$ is illustrated in Fig. 2 on a 2D slice of the upsampled thalamus computed in 3D, as well as the corresponding $\phi_L$, $\phi_F$ and $\phi_S$ in the right column. Notice that the color schemes for $L$, $F$, $S$ and $T$ in the figures correspond to the underlying objects, i.e., $F$ in one color is the first neighbor of the region in the same color in $L$, while $S$ is the second neighbor of that same-colored region of $L$.

Using this decomposition, one can reconstruct some parts of the the underlying signed distance function of object $O_i$ as follows:

$$\varphi_i(x) = \begin{cases} \phi_L(x), & L(x)=i; \\ -\phi_L(x), & F(x)=i; \\ -\phi_L(x) - \phi_F(x), & S(x)=i; \\ -\phi_L(x) - \phi_F(x) - \phi_S(x), & T(x)=i; \\ \text{unknown}, & \text{otherwise}. \end{cases} \tag{4}$$

Although the reconstruction is not known everywhere, it is sufficient for surface evolution when using a narrow band [19] technique. We will approximate the level set function in the unknown regions as $-\phi_L(x) - \phi_F(x) - \phi_S(x)$, so that:

$$\tilde{\varphi}_i(x) = \begin{cases} \phi_L(x), & L(x)=i; \\ -\phi_L(x), & F(x)=i; \\ -\phi_L(x) - \phi_F(x), & S(x)=i; \\ -\phi_L(x) - \phi_F(x) - \phi_S(x), & \text{otherwise} \end{cases} \tag{5}$$

Actually although not the exact signed distance function, Eq. 5 is a level set function of $O_i$, satisfying Lipschitz continuity, and positive inside the region while negative outside.

### 2.2. Evolution

Given the compact decomposition of the level set functions into $\phi_L$, $\phi_F$ and $\phi_S$, the evolution of any individual level set function $\varphi_i$ according to the overall forces $f_i$ applied on $O_i$ can be recast as the evolution of $\phi_L$, $\phi_F$ and $\phi_S$ and the labels $L$, $F$ and $S$[1].

The evolution of the labels depend on the change of sign in the corresponding functions. Suppose for voxel $x$, $L(x) = i$, $F(x) = j$ and $S(x) = k$. By definition, we require $\phi_L > 0$, so whenever $\phi_L < 0$ at voxel $x$, $L(x)$ must be changed to another label. The only valid candidate is the first neighbor $\hat{j}$, assuming $O_{\hat{j}}$ is the first closest neighbor to $x$ in the current segmentation, whose identity may change during the evolution of $\phi_F$. The evolution of the boundary between $i$ and $\hat{j}$ depends on which region has a stronger expanding force, so the evolution of $\phi_L$ is

$$\frac{\partial \phi_L}{\partial t} = \frac{1}{2}(f_i - f_{\hat{j}}) \tag{6}$$

During the evolution, it is necessary to make sure that the first neighbor is the nearest neighbor, as the configuration of neighbors changes along with changes in $L$. Frequent reinitialization can ensure a correct configuration, but this is time consuming and inelegant. Instead, we can evolve $\phi_F$ and $\phi_S$ so that all the labels remain consistent. At any time, the competition to be the updated first closest neighbor is between the original first closest neighbor $j$, and the second closest neighbor $\hat{k}$. In other words, if $\phi_F < 0$, then the first and second closest neighbors must switch. The evolution of $\phi_F$ is similar to the evolution of $\phi_L$:

$$\frac{\partial \phi_F}{\partial t} = \frac{1}{2}(f_j - f_{\hat{k}}). \tag{7}$$

But where does $\hat{k}$ come from? All the regions neighboring $i$, except $j$ and $k$, are competing with $k$ to be the second neighbor $\hat{k}$. Of all the candidates, the one that possesses the strongest expanding force on $x$ is the best candidate for the second closest neighbor. Accordingly, the evolution of $\phi_S$ is

$$\frac{\partial \phi_S}{\partial t} = \frac{1}{2}(f_k - \max_{l \neq i,j,k} f_l). \tag{8}$$

Like $L$ and $F$, the second closest neighbor at $x$ must change from $k$ to arg $\max_{l \neq i,j,k} f_l$ when $\phi_S < 0$.

Note that this evolution method is dependent on the dimensionality of the image. In 2D, only $L$ and $F$ are necessary as there is no non-singular boundary with more than three objects. To generalize the framework in even higher dimensions, we would need to add a third neighbor, fourth neighbor, and so on.

---

[1] Since the approximation of the recovery is used by Eq. 5, it is unnecessary to keep track of $T$.

Note that our approach derives everything in the level set framework; therefore, efficient schemes from the level set literature can be readily used. In the following experiments, the fast marching method [19] is used for initialization, while the narrow band algorithm is used for fast evolution.

For medical applications, we are usually interested in applying topological constraints that are known a priori, as the objects to segment follow standard anatomy. Topology constraints can be incorporated seamlessly in our framework by modifying slightly the evolution of $\phi_L$: when $\phi_L$ would change from positive to negative, and if the topology constraints for the new segmentation given by $L$ are not respected, then the label is left unchanged and the function is reset to a small value $\varepsilon > 0$. To preserve the topology of groups of objects, we must use the digital homeomorphism constraint (DHC) of [29] as it guarantees to preserve the topology of both the objects and their relationships.

In summary, $\forall x$ in which $L(x) = i$, $F(x) = j$ and $S(x) = k$, the multi-compartment geometric deformable model (MGDM) algorithm is:

1. find $\hat{l} = \arg\max_{l \neq i,j,k} f_l$, with $O_l$ neighbor of $O_i$,
2. compute $\frac{\partial \phi_S}{\partial t} = \frac{1}{2}(f_k - f_{\hat{l}})$, if $\phi_S + \frac{\partial \phi_S}{\partial t} < 0$, change $S(x)$ from $k$ to $\hat{l}$. The updated second closest neighbor is $\hat{k}$.
3. Compute $\frac{\partial \phi_F}{\partial t} = \frac{1}{2}(f_j - f_{\hat{k}})$. If $\phi_F + \frac{\partial \phi_F}{\partial t} < 0$, change $F(x)$ from $j$ to $\hat{k}$ and $S(x)$ from $\hat{k}$ to $j$. The updated first closest neighbor is $\hat{j}$.
4. Compute $\frac{\partial \phi_L}{\partial t} = \frac{1}{2}(f_i - f_{\hat{j}})$, if $\phi_L + \frac{\partial \phi_L}{\partial t} < 0$ the DHC allows, change the label $L(x)$ from $i$ to $\hat{j}$ and first neighbor $F(x)$ from $\hat{j}$ to $i$, otherwise set $\phi_L = \varepsilon$.

Compared with the $N$ level sets approach, our method is significantly more efficient, with a fast marching initialization in $O(\frac{n^3}{N}\log\frac{n}{N})$ and a narrow band evolution in $O(\varepsilon n^2)$ time, where $n$ is the number of grid points along one dimension and $\varepsilon$ the narrow band width (see [38]).

## 3. Experiments

### 3.1. Whole Brain Segmentation

We applied this framework to the segmentation of the whole brain into ten separate structures: cerebral and cerebellar gray and white matter, sulcal cerebro-spinal fluid (CSF), ventricles, caudate, putamen, thalamus, and brain stem. We first used an atlas-based classification algorithm to get membership functions for each object and a (voxel-accurate) segmentation with the desired topology [28]. MGDM is then used to smooth the boundaries and yield sub-voxel accuracy, in analogous fashion to that of [20]. The memberships are used in a balloon image-guiding force, and the boundary is regularized by a curvature smoothing force, as follows

$$f_i = (0.5 - F_i)|\nabla\varphi| + \kappa|\nabla\varphi|, \tag{9}$$

in which $F_i$ is the membership function of region $O_i$, $\kappa$ is the curvature, and $f_i$ the force acting on region $O_i$. It takes 45 minutes in 120 iterations on the data set of size 256 * 256 * 205 for the algorithm to converge. In Figs. 3 and 4, we compare four segmentation results, first using only the balloon forces or the balloon and curvature forces and no topology constraint, then adding a single object topology constraint as in [40] and finally using the homeomorphic constraint of [29].

It is apparent that without any topological constraint, the segmentation connects the cerebrum and cerebellum together, while the CSF is supposed to separate them. Even with topological constraints on each separate object, including the CSF, this connection is still possible because the CSF sheet can move in 3D at the interface. As expected, the smoothing "cleans up" the smaller regions and produces a much smoother boundary (see Fig. 3). To better analyze the result in 3D and to see the relationships between objects, we visualized three objects—ventricle in red, caudate in green, and thalamus in blue—in Fig. 4. 3D visualization provides us a clear view of the little spots disconnected from the whole tissue when no topological constraint is applied. The single-object topological constraint results in the thalamus and caudate being connected, while the homeomorphic constraint guarantees the relationship between objects is the same throughout the evolution, comparing the enlarged pictures of the black box in Fig. 4. The Euler number has been checked, and they remain the same during the evolution.

### 3.2. Thalamic Nuclei Parcellation

The second experiment focuses on thalamic nuclei parcellation using diffusion tensor MRI (DT-MRI). Because of the added information derived from the diffusion tensors, it is possible to differentiate the nuclei that are otherwise indistinguishable in structural images. This application is challenging due to the large number of small regions that must be simultaneously segmented (13 in each hemisphere), and the complex topological relationships between them. Previous works obtained promising results with K-means clustering modeling the diffusion in the cluster distance metric [12], using a normalized cuts spectral clustering approach [41], or introducing a region force driven by diffusion tensors belonging to the region in a level set framework [21]. All these methods are based on the hypothesis that the fiber orientations are homogeneous inside each nucleus but differ between different nuclei. No previous approach addressed the issue of topology preservation.

In this experiment, we start with a whole brain segmentation (see [28]) using a standard MP-RAGE image of the brain [Fig. 5(a)], yielding (among other things) a membership function corresponding to the thalamus [Fig. 5(b)]. Diffusion tensors of a co-registered DT-MRI image are then estimated and the primary eigenvector (PEV) and fractional anisotropy (FA) are computed from the diffusion tensors [Figs. 5(c) and (d)].

To parcellate the thalamus according to the directional homogeneity inside each nucleus, we designed a force in the fashion of the Chan-Vese model [35] (very similar to that of [21]). Because MGDM compares the forces from neighboring regions, however, only the diffusion tensor forces of the current nucleus are needed to evolve $\phi_L$, $\phi_F$, $\phi_S$, as follows

$$f_i(\mathbf{x}) = |\mathbf{v}(\mathbf{x}) - \mathbf{V}_i| \tag{10}$$

where $\mathbf{v}$ is the principal orientation for the current voxel, $\mathbf{V}_i$ is the mean principal orientation from region $i$, and $f_i(\mathbf{x})$ is the force at voxel $\mathbf{x}$ from region $i$.

The diffusion tensors change smoothly when leaving the thalamus toward the neighboring white matter, so a balloon force from the membership function of the segmented thalamus is needed to maintain the outer boundary of the thalamus. At the same time, the DTI-based force of Eq. (10) is used to parcellate the nuclei inside the thalamus. Thus, the forces used at the boundary of each nucleus depend on whether the neighboring region is a nucleus or the extra-thalamic region. An initial topologically correct parcellation was taken from the ICBM atlas [1] [Fig. 5(e)] and aligned to the underlying thalamus.

The resulting segmentation is shown in Fig. 5(f). Comparing the Figs. 5(b), (e), and (f), one can see that the final thalamus shape is correct and its final regions correspond well to the orientations that one sees in the PEV's. The algorithm takes only several minutes for a 256*256*173 data set by cropping out and dealing with the thalamus of size 61*54*48. A 3D view of the 26 nuclei is given in Fig. 6. As long as the topological relationship between nuclei is correct in the initialization, it will not change during the evolution because of the homeomorphic constraint.

## 4. Conclusion

We presented a novel multiple object segmentation framework utilizing level sets that is well suited to 3D medical images. The compact representation is computationally efficient, guarantees there is no overlap or vacuum among objects, and allows us to preserve the global topology of the segmentation at all times. Any existing force in the level set literature can be incorporated in our MGDM algorithm, and different forces can be applied to different parts of each object. Applications to whole brain segmentation and thalamic parcellation illustrate the capacity of MGDM to include different forces, with or without topological constraint on one or multiple objects. The thalamus experiment further demonstrates how the framework can successfully handle many interacting objects, and how the need for different forces on different parts of an object arises quite naturally in the design of a segmentation method.

## Acknowledgments

This work is supported by NIH/NINDS grant R01 NS56307 and NIH/NINDS grant R01 NS37747.

## References

1. In http://www.loni.ucla.edu/ICBM/.
2. Mansouri A, Mitiche A, Vzquez C. Multiregion competition: A level set extension of region competition to multiple region image partitioning. Comp Vis and Imag Underst. 2006; 101:137–150.
3. Tsai A, Wells W, Tempany C, Grimson E, Willsky A. Mutual information in coupled multi-shape model for medical image segmentation. Med Imag Anal. 2004; 8:429–445.
4. Yezzi A, Tsai A, Willsky A. A fully global approach to image segmentation via coupled curve evolution equations. J of Vis Comm and Imag Repres. 2002; 13:195–216.
5. Bischoff S, Kobbelt L. Sub-voxel topology control for level-set surfaces. Computer Graphics Forum. 2003; 22(3):273–280.
6. Samson C, Blanc-Fraud L, Aubert G, Zerubia J. A level set model for image classification. Scale-Space Theories in Computer Vision. 1999:306–317.
7. Xu C, Prince JL. Snakes, shapes, and gradient vector flow. IEEE Trans Imag Proc. 1998; 7:359–369.
8. Zimmer C, Olivo-Marin Jean-Christophe. Coupled parametric active contours. IEEE Trans PAMI. 2005; 27:1838–1842.
9. Cremers D, Rousson M, Deriche R. A review of statistical approaches to level set segmentation: Integrating color, texture, motion and shape. Int'l J Comp Vis. 2007; 72:195–215.
10. Cremers D, Osher S, Soatto S. Kernel density estimation and intrinsic alignment for shape priors in level set segmentation. Int'l J Comp Vis. 2006; 69:335–351.
11. Mumford D, Shah J. Optimal approximation by piecewise smooth functions and associated variational problems. Comm Pure Appl Math. 1989; 42:577–685.
12. Tuch, DS. PhD thesis. Division of Health Sience and Techonology; Yale: 2002. Diffusion MRI of Complex Tissue Structure.

13. Angelini, E.; Song, T.; Mensh, B.; Laine, A. Multi-phase three-dimensional level set segmentation of brain MRI. MICCAI; 2004. p. 318-326.
14. Sgonne F, Pons JP, Grimson E, Fischl B. Active contour under topology control - genus preserving level sets. Proc CVBIA. 2005; 2005:135–145.
15. Sgonne, F.; Eric, W.; Fischl, B. Topological correction of subcortical segmentation. MICCAI; 2003. p. 695-702.
16. Fischl B, Salat DH, Busa E, Albert M, Dieterich M, Haselgrove C, van der Kouwe A, Killiany R, Kennedy D, Klaveness S, Montillo A, Makris N, Rosen B, Dale AM. Whole brain segmentation: Automated labeling of neuroanatomical structures in the human brain. Neuron. 2002; 33:341–355. [PubMed: 11832223]
17. Zhao H, Chan T, Merriman B, Osher S. A variational level set approach to multiphase motion. J of Comp Phys. 1996; 127:179–195.
18. Heimann, T.; Munzing, S.; Meinzer, H-P.; Wolf, I. A shape-guided deformable model with evolutionary algorithm initialization for 3d soft tissue segmentation. Proceedings of the International Conference on Information Processing in Medical Imaging 2007 (IPMI'07); Kerkrade. july 2007;
19. Sethian, JA. Level set methods: evolving interfaces in geometry, fluid mechanics, computer vision, and materials science. Cambridge: Cambridge University Press; 1996.
20. Pohl, K.; Kikinis, R.; Wells, W. Active mean fields: Solving the mean field approximation in the level set framework. IPMI; 2007. p. 26-37.
21. Jonasson L, Hagmann P, Thiran J. A level set method for segmentation of the thalamus and its nuclei in DT MRI. Signal Processing. 2007; 87(2):309–321.
22. Vese L, Chan TF. A multiphase level set framework for image segmentation using the mumford and shah model. Int'l J Comp Vis. 2002; 50:271–293.
23. Kass, AM.; Terzopoulos, D. Snakes: Active contour models. IJCV; 1988. p. 321-331.
24. Leventon WM, Faugeras O. Statistical shape influence in geodesic active contours. Proceedings of CVPR. 2000:316–323.
25. Rousson M, Paragios N. Shape priors for level set representation. Proceeding of ECCV. 2002:78–93.
26. Paragios, N.; Deriche, R. Coupled geodesic active regions for image segmentation: A level set approach. ECCV; 2000. p. 224-240.
27. Okada, T.; Shimada, R.; Sato, Y.; Hori, M.; Yokota, K.; Nakamoto, M.; Chen, Y-W.; Nakamura, H.; Tamura, S. Automated segmentation of the liver from 3d ct images using probabilistic atlas and multi-level statistical shape model. MICCAI; 2007. p. 86-93.
28. Bazin, P-L.; Pham, DL. Statistical and topological atlas based brain image segmentation. Proceedings of the 9th International Conference on Medical Image Computing and Computer-Assisted Intervention (MICCAI'07); Brisbane. october 2007;
29. Bazin, P-L.; Ellingsen, L.; Pham, DL. Digital homeomorphisms in deformable registration. IPMI; 2007. p. 211-222.
30. Pham D, Xu C, Prince J. Current methods in medical image segmentation. Annual Review of Biomedical Engineering. 2000; 2:315–337. Annual Reviews.
31. Osher S, Sethian JA. Fronts propagating with curvature dependent speed: Algorithms based on hamilton-jacobi formulations. Journal of Computational Physics. 1988; 79:12–49.
32. Osher, S.; Fedkiw, R. Level set methods and dynamic implicit surfaces. New York: Springer; 2003.
33. Sundaramoorthi G, Yezzi AJ. Global regularizing flows with topology preservation for active contours and polygons. IEEE Transactions on Image Processing. 2007; 16(3):803–812. [PubMed: 17357738]
34. Brox T, Weickert J. Level set segmentation with multiple regions. IEEE Trans Imag Proc. October; 2006 15(10):3213–3218.
35. Chan T, Vese L. Active contours without edges. IEEE Trans Imag Proc. 2001; 10:266–277.
36. Caselles V, Kimmel R, Sapiro G. Geodesic active contours. Intl J Comp Vision. 1997; 22:61–79.

37. Bresson PX, Thiran JP. A prior information in image segmentation: energy functional based on shape statistical model and image information. Proceeding of ICIP. 2003:425–428.

38. Fan X, Bazin P-L, Prince JL. A multi-compartment segmentation framework with homeomorphic level sets. Proceeding of CVPR. 2008

39. Han X, Xu C, Prince JL. Topology correction in brain cortex segmentation using a multi-scale, graph-based algorithm. IEEE Trans Med Imaging. 2002; 21(2):109–121. [PubMed: 11929099]

40. Han X, Xu C, Prince JL. A topology preserving level set method for geometric deformable models. IEEE Trans Patt Anal Machine Intell. 2003; 25:755–768.

41. Ulas, DZ.; Westin, C. Segmentation of thalamic nuclei from dti using spectral clustering. MICCAI; 2006. p. 807-814.

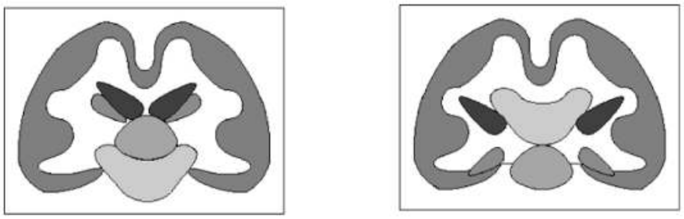

**Figure 1.**

Illustration of the homeomorphic constraint: if there is no constraint on the topology of groups of objects, then the organs can slide freely and exchange place during evolution, though each one may keep its own topology.

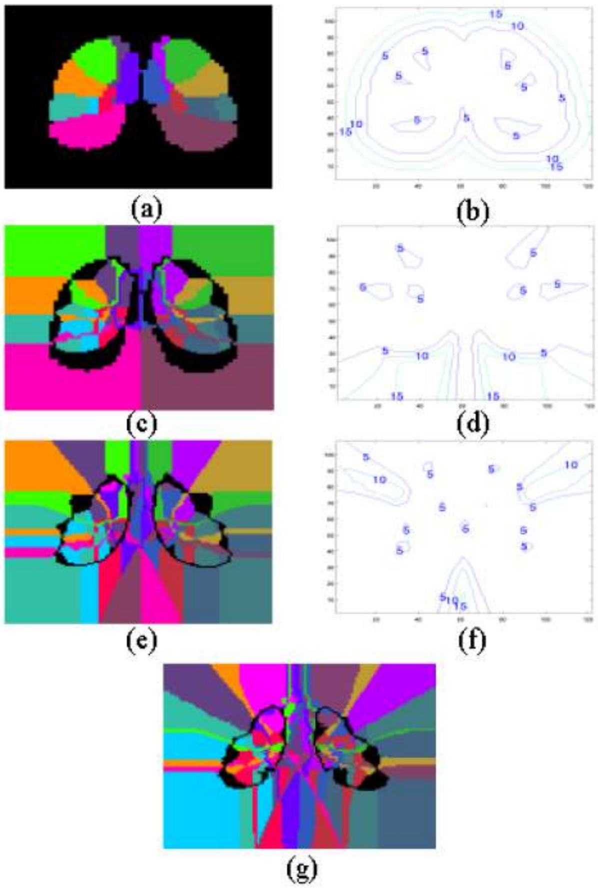

**Figure 2.**

Illustration of $L$, $F$, and $S$ in the decomposition of an object: (a) $L$, (b) $\phi_L$, (c) $F$, (d) $\phi_F$, (e) $S$, (f) $\phi_S$, (g) $T$.

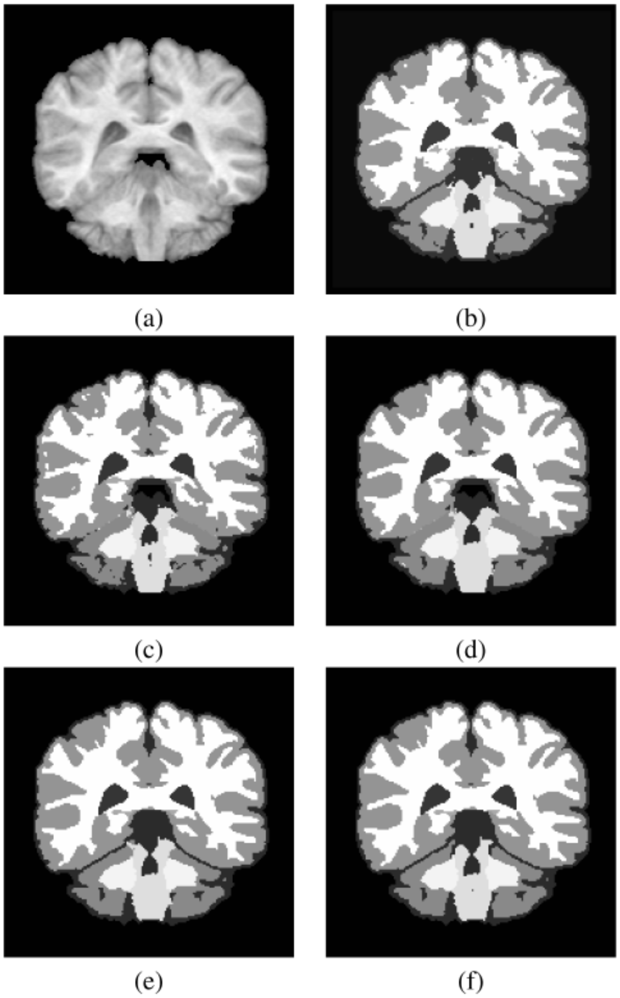

(a) (b)

(c) (d)

(e) (f)

**Figure 3.**

Whole brain segmentation: (a) source image, (b) original segmentation result, and MGDM result with (c) no smoothing or topology constraint, (d) smoothing and no topology constraint, (e) smoothing and single object topology constraint, and (f) smoothing and homeomorphic constraint.

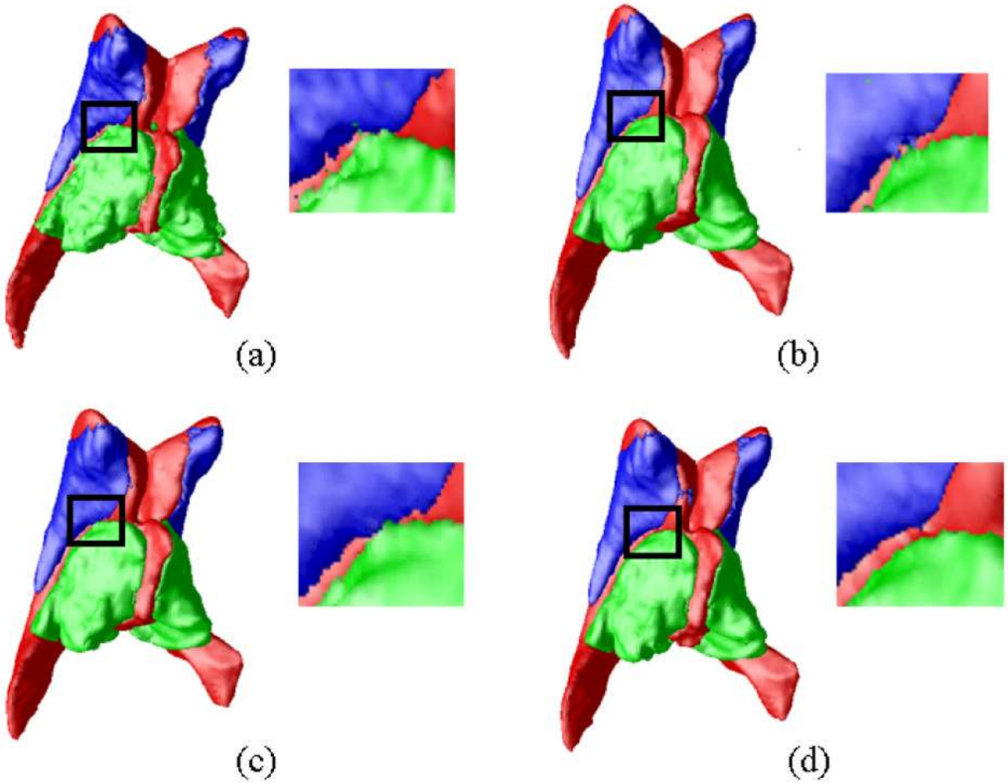

**Figure 4.**

3D visualization of whole brain segmentation results for ventricles (red), caudate (green) and thalamus (blue): a) with no topology constraint, no smoothing, b) with smoothing, but no topology constraint, c) with smoothing and single object topology constraint, d) with smoothing and homeomorphic constraint.

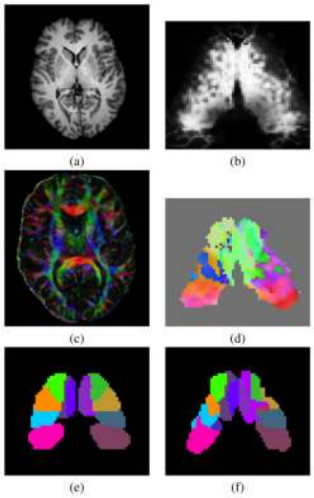

**Figure 5.**

Thalamic nuclei parcellation: (a) mprage image coregistered with FA, (b) membership function for the thalamus, (c) FA image with a principal eigenvector color map, (d) principal orientation with only the thalamus left, (e) initialization with 26 regions, (f) final parcellation result.

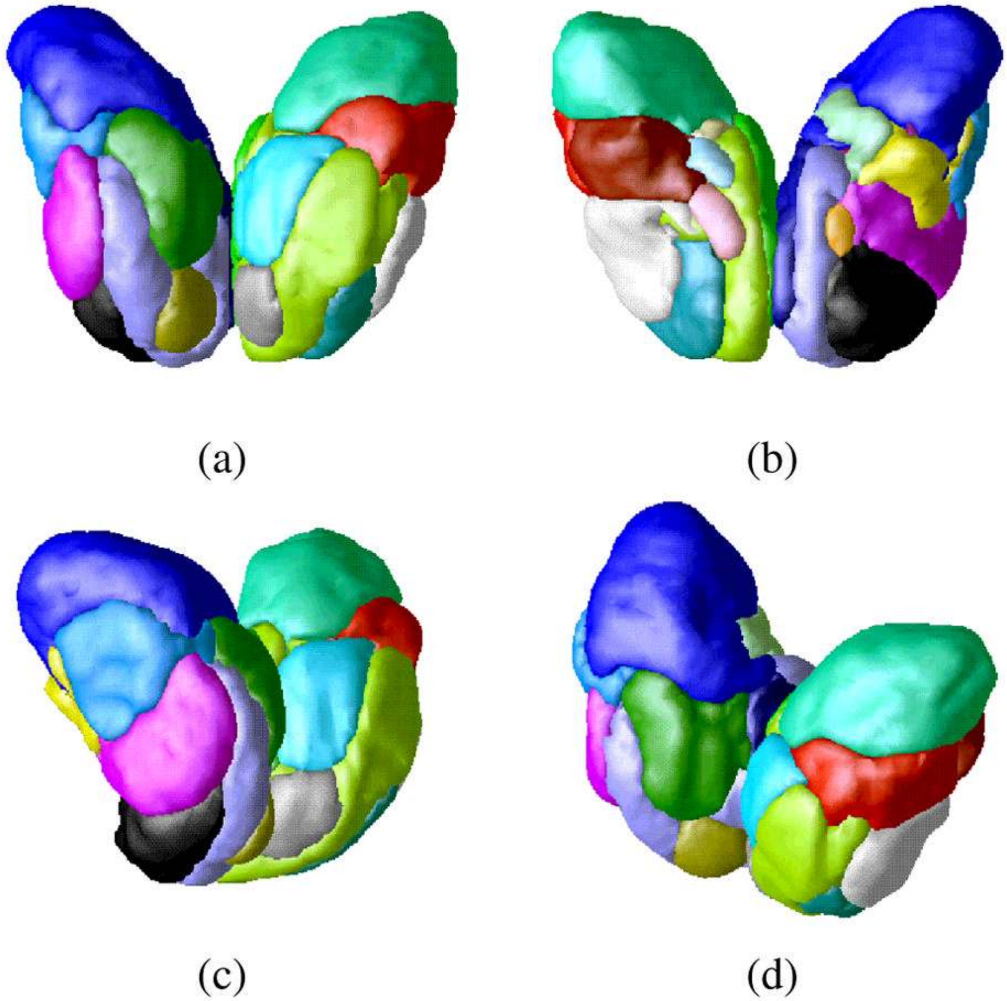

(a) (b)

(c) (d)

**Figure 6.**
3D rendering of the thalamic nuclei parcellation result: (a) front view, (b) back view, (c) off left view, (d) off diagonal view.